Numerical Solution of EMHD GO-Fe_3O_4/H_2O Flow and Heat Transfer over Moving Riga Plate with Thermal Radiation and Heat Absorption/Generation Impacts

Nooraini Zainuddin[1, a)], Nor Ain Azeany Mohd Nasir[2, b)] , Norli Abdullah[3, c)] and Anuar Ishak[4, d)]

Author Affiliations

[1]*Department of Fundamental and Applied Sciences, Faculty of Science and Information Technology, Universiti Teknologi PETRONAS, 32610 Seri Iskandar, Perak, Malaysia.*

[2]*Department of Mathematics, Centre for Defence Foundation Studies, Universiti Pertahanan Nasional Malaysia, Kem Sungai Besi 57000 Kuala Lumpur, Malaysia.*

[3]*Department of Chemistry and Biology, Centre for Defence Foundation Studies, Universiti Pertahanan Nasional Malaysia, Kem Sungai Besi 57000 Kuala Lumpur, Malaysia.*

[4]*Department of Mathematical Sciences, Faculty of Science and Technology, Universiti Kebangsaan Malaysia, 43600 UKM Bangi, Selangor, Malaysia.*

Author Emails

[a)]aini_zainuddin@utp.edu.my

[b)] Corresponding author: norainazeany@upnm.edu.my

[c)]norli.abdullah@upnm.edu.my

[d)]anuar_mi@ukm.edu.my

Abstract. The importance of thermal radiation impacts on electromagnetohydrodynamics (EMHD) hybrid nanofluid movement and heat transference towards stretching/shrinking surface is investigated. The influences of external effects such as suction, heat absorption and generation are also being considered. The hybrid nanofluid chosen for exploration is Graphene Oxide (GO) and Iron Oxide (Fe_3O_4) as nanoparticles, while water (H_2O) is a base fluid. The mathematical modelling in partial differential equations (PDEs) is formulated to ordinary differential equations (ODEs) for simplicity using an appropriate similarity variable. The solution of the reduced ODEs is then computed with the help of bvp4c solver built-in MATLAB software. The findings reveal that the magnetic field augmented the velocity profile, while thermal radiation affects the temperature profiles to amplify. The heat generation and absorption upsurged the heat transfer for GO-Fe_3O_4/H_2O with accompanying effects like plate thickness. It is also worth mentioning that GO-Fe_3O_4/H_2O enhanced skin friction and heat transfer by about 3.2% and 1.6%, respectively, more than Fe_3O_4/H_2O.

INTRODUCTION

In the past few decades, research on optimising thermal efficiency has been continually growing. This topic of interest includes the nanofluid exertion being a lubricant that can cool down heated systems, which gives a cheap extraordinary thermal efficacy. A Nanofluid is a nanoparticle base fluid, a mixture of a single nanoparticle in a base fluid. The base fluids are frequently chosen as water, ethylene glycol (EG), or other fluids, and the nanoparticles can be metals or metal oxides such as carbon nanotubes or graphene [1, 2, 3]. Study of nanofluid in improving thermal efficiency includes [4, 5, 6].

Due to its good performance in terms of heat transfer, scientists proposed a hybrid nanofluid with more excellent heat conductivity than a conventional single-type nanofluid. When multiple types of nanoparticles are combined with the base fluid, the result is a hybrid nanofluid. The combination strengthens each nanoparticle's capability and

compensates for flaws to achieve the ideal heat transmission ratio. A hybrid nanofluid Ag-MWCNT/H_2O has been studied by Sun et al. [7]. According to the findings, Ag-MWCNT/H_2O have more excellent thermal conductivity than MWCNT nanofluids. Sahoo [8] addressed the water-based tripartite Al_2O_3-SiC-TiO_2 hybrid nanofluids by abusing a two-stage process. The results showed that low volume fraction had a minor effect on the hybrid nanofluid's viscosity, whereas high volume fraction increased the fluid's internal resistance. The heat transfer properties of aquatic $ZnFe_2O_4/H_2O$ nanofluids are investigated by Gupta et al. [9]. The effectiveness of the coupling of carboxyl graphene and graphene oxide was investigated by Ponangi et al. [10]. They claimed that the combination of hybrid nanofluid makes graphene oxide nanoparticles more effective, with an average increase in efficacy from 86% to 132% when the concentration amount of graphene oxide is changed from 0.0025% to 0.005%. The water-based hybrid nanofluids of Al_2O_3-TiO_3, Cu-Al_2O_3, and Cu-TiO_2 have been studied by Hussain et al. [11]. Their research shows that by enhancing viscous dissipation and radiation effects, the temperature of the hybrid nanofluid may be raised. The use of suction and radiant heat can also improve heat transmission. In contrast, the aftermath of the magnetic field, injection, thermal slip factor, and viscous dissipation on hybrid nanofluid's heat transfer rate are all important.

Graphene, a carbon nanomaterial, combines luminosity, chemical stability, a large surface area, excellent mechanical and electrical properties, and thermal conductivity to generate better thermally conductive nanofluids [12]. According to Balandin et al. [13], the claim made by Sur [12] can further improve the nanofluid characteristic with Graphene as the nanometal. Graphene oxide (GO), reduced graphene oxide (rGO), double- or triple-layered graphene, graphene nanoplatelets, and functional graphene are all derivatives of graphene that find widespread use in industrial and commercial settings [14], [15]. Graphene nanofluids have high heat conductivity and can be used as insulation for solar energy collection. Mahanta and Abramson [16] investigated the conductivity of graphene and graphene oxide nanofluids. The enhanced heat conductivity of multilayered graphene was attributed to their discovery that oxygen atoms induce covalent interlayer interactions. Liu et al. [17] created an ionic liquid-based graphene nanofluid and used it to test the efficiency of a solar collector. They found that by incorporating graphene nanoparticles into fluids, radiation absorption could be improved. A high concentration of graphene was also found to have an effect on the efficiency of the solar energy system. Meanwhile, Torii [18] has proposed GO-H_2O flow in horizontal tubes and heated pipes for cooling purposes. The finding showed that the thermal performance of a heat pipe is enhanced as the concentration of GO nanoparticles in the base fluid is increased. Nasir et al. [19] reveal that MoS_2-GO as nanometal exhibits the highest level of efficiency.

Hydrothermal properties of nanofluid movement are essential to study because thermal radiation plays a crucial role in regulating the ambient temperature of the nanofluid flow. Masuda et al. [20] were the first group to use significantly conducting nanoparticles to increase the thermal conductivity of the heat transfer fluid. Since then, many different aspects of heat transmission have been investigated. These include magnetic fields, porous media, dissimilar plate surfaces, thermal radiation, viscosity, thermal generation, and absorption. Sun et al. [21] continued to work on the features of ferro-nanofluid transferring heat, and Walvekar et al. [22] looked into how carbon nanotube nanofluid's turbulence transfers heat. Reddy and Chamkha [23] investigated the effects of Soret and Dufour in nanofluids exposed to porous media with heat generation or absorption. Khan et al. [24], who investigated the impact of heat production and absorption on the Falkner-Skan flow of Carreau nanofluid, are just one group of researchers looking into this phenomenon. Ishaq et al. [25] used irreversibility treatment to examine the effects of thermal radiation on the migration of a magnetohydrodynamic (MHD) nanofluid. Unsteady free convection MHD flow through a permeable medium was investigated for heat production, absorption, and thermodiffusion by Veera and Chamkha [26]. Oudina [27] studied the convective heat energy transfer during the nanofluid, while Waqas et al. [28] revealed that the thermal distribution profile exhibits an enhanced performance as the Biot number and thermal radiation values increase. Rashad et al. [29] reported that as the enhancement of thermal radiation and heat generation occurred, there was an observed rise in heat transmission.

From the aforementioned studies, we can deduce that only a few researchers are occupied with investigating hybrid nanofluid flow, GO as nanoparticles, and heat transfer over shrinking Riga plates (or electro-magnetohydrodynamics, or EMHD). Due to this gap, the current study seeks to investigate the effects of heat production, consumption, and emission on EMHD hybrid nanofluid flow and heat transfer towards highly permeable stretching and contracting Riga plates at the stagnation point. The GO-Fe_3O_4 hybrid nanofluid particles and water were selected for this study. The findings of this study can provide insights into the design and optimisation of EMHD hybrid nanofluid-based heat transfer systems for various industrial applications. Furthermore, the outcomes of this investigation hold the promise of contributing to the development of sustainable and energy-efficient technologies. This pursuit aligns seamlessly with the broader goals of scientific and technological advancement. The results may also contribute to the development of sustainable and energy-efficient technologies. The mathematical modelling for the investigation is constructed in partial differential equations (PDEs) and further reduced into systems of ordinary differential equations (ODEs) to

make solving the mathematical modelling less complex. The reduced ODEs are obtained using appropriate similarity variables. The reduced ODEs are solved by a built-in solver in MATLAB called bvp4c. The solutions are then analysed and discussed thoroughly.

MATHEMATICAL MODELING

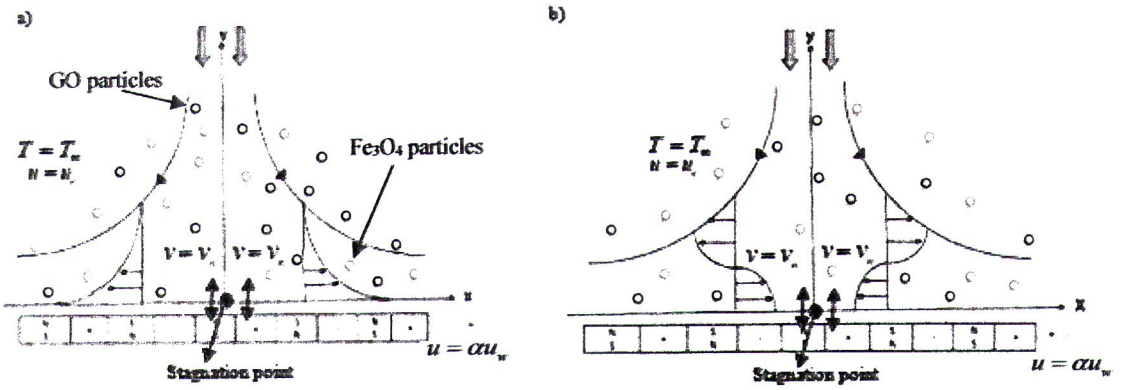

FIGURE 1. Physical model and coordinate system for (a) stretching Riga plate $(\alpha > 0)$ and (b) shrinking Riga plate $(\alpha < 0)$.

Assume that a two-dimensional steady boundary layer flow moved toward a permeable Riga plate surface with exerted impact such as radiation, suction and heat absorption/generation, as pictured in Fig. 1. The x and y coordinates are regulated as a companion of the stretched and shrunk Riga plate surface. It is also presumed that the GO-Fe_3O_4/H_2O flow starts at $y \geq 0$. The Riga plate surface is supposed to move in the x-direction defined as $u(x) = \alpha u_w(x)$ with the positive α noted as stretched Riga plate surface and the negative α prominent as shrunk Riga plate surface. Infer that $v(x) = v_w$ is pointed out as the mass velocity when v_w is positive, which means that suction while v_w is negative, denoted as injection parameters. The surface temperature is known as T_w and T_∞ is defined as ambient temperature. From the above assumption, the governing boundary layer can be constructed as follows (see Supian et al. [30]):

$$\frac{\partial u}{\partial x} + \frac{\partial v}{\partial y} = 0 \tag{1}$$

$$u\frac{\partial u}{\partial x} + v\frac{\partial u}{\partial y} = u_e\frac{du_e}{dx} + \frac{\mu_{hnf}}{\rho_{hnf}}\frac{\partial^2 u}{\partial y^2} + \frac{\pi j_0 M_0}{8\rho_{hnf}}e^{\frac{\pi}{\alpha_1}y} \tag{2}$$

$$u\frac{\partial T}{\partial x} + v\frac{\partial T}{\partial y} = \frac{k_{hnf}}{(\rho C_p)_{hnf}}\left(\frac{\partial^2 T}{\partial y^2}\right) + \frac{Q_0}{(\rho C_p)_{hnf}}(T - T_\infty) - \frac{1}{(\rho C_p)_{hnf}}\left(\frac{\partial q_r}{\partial y}\right) \tag{3}$$

along with a suitable boundary layer

$$\begin{aligned} u = \alpha u_w, \quad v = v_w(x), \quad T = T_w(x) \quad at\ y = 0 \\ u \to u_e = ax, \quad T \to T_\infty \quad as\ y \to \infty \end{aligned} \tag{4}$$

It is worth mentioning that the component GO-Fe_3O_4/H_2O velocity is accompanied by x, and y axes are denoted as u and v respectively. The governing equations (1)-(4) will be solved using the numerical method of ordinary differential equations. Hence, it is crucial to reduce the equations (1)-(4) into ordinary differential equations. The facilitated process is done using an appropriate similarity transformation. The suitable similarity transformation is introduced as follows (see Nasir et al. [31]):

$$u = axf'(\eta), \quad v = -\sqrt{ab_f}f(\eta), \quad h(\eta) = \frac{T - T_\infty}{(T_w - T_\infty)}, \quad \eta = y\sqrt{\frac{a}{b_f}} \tag{5}$$

The equation (5) is substituted into the governing equations (1)-(4) hence will produce a new form of ordinary differential equations as follows.

$$\frac{\varphi_a}{\varphi_b} f''' - f'^2 + f f'' + 1 + \left(\frac{Q}{\varphi_b}\right) e^{-\eta\omega} = 0 \tag{6}$$

$$\left(\frac{\varphi_c}{\varphi_d} + \frac{\chi}{\varphi_d}\right)\mathrm{Pr} h'' + f h' + \frac{\psi}{\varphi_d} h = 0 \tag{7}$$

tagging with an appropriate boundary condition

$$\begin{aligned} f'(0) = \alpha, \quad f(0) = S, \quad h(0) = 1 \quad \text{at} \quad \eta = 0 \\ f'(\eta) \to 1, \quad h(\eta) \to 0 \quad \text{as} \quad \eta \to \infty \end{aligned} \tag{8}$$

It is noted that the hybrid nanofluid parameters involved in equations (6)-(8) are defined as $\varphi_a = \frac{\mu_f}{\mu_{hnf}}$, $\varphi_b = \frac{\rho_{hnf}}{\rho_f}$, $\varphi_c = \frac{k_{hnf}}{k_f}$ and $\varphi_d = \frac{(\rho C_p)_{hnf}}{(\rho C_p)_f}$. The associated formulas for computing the value of hybrid nanofluid parameters $\varphi_a, \varphi_b, \varphi_c, \varphi_d$ are listed in Table 1. Table 1 displays the corresponding thermos physical features formula for finding the value of the hybrid nanofluid parameters. The value of thermo-physical properties for GO-Fe_3O_4/H_2O hybrid nanofluid particles is archived in Table 2. These values will be used to calculate the hybrid nanofluid parameters $\varphi_a, \varphi_b, \varphi_c, \varphi_d$. It is noted that the subscript $hnf, nf, f, s1, s2$ is known as hybrid nanofluid, nanofluid, base fluid, first nanoparticle and second nanoparticle, respectively. The other parameters entangled with the equation (6)-(8), such as $\omega = \frac{\pi}{\alpha_1}\sqrt{\frac{b_f}{a}}$ known as a dimensionless parameter allied with the electrode and magnet of the Riga plate thickness, the radiation is identified as $\chi = \frac{16\sigma^* T_\infty^3}{3\kappa^* k_f}$, $\psi = \frac{Q_0}{a(\rho C_p)_f}$ is recognised as a heat source when the value is positive, and heat sink as the value is negative as well as $Q = \frac{\pi j_0 M}{8a^2 \rho_f}$ familiar as modified Hartmann number or EMHD parameter. The Prandtl number is denoted as $\mathrm{Pr} = \frac{k_f}{b_f(\rho C_p)_f}$ and $S = -\frac{v_0}{\sqrt{ab_f}}$ is established as a suction parameter when the value is positive, while notorious as an injection when the value is negative.

The skin friction coefficient c_f represents the drag force acting on a fluid flowing over a surface. At the same time, the Nusselt number Nu_x characterises the convective heat transfer between a fluid and a solid surface. These parameters are essential in many engineering applications, such as aerodynamics and heat exchanger design. c_f and Nu_x are given as,

$$c_f = \frac{\tau_w}{\rho U_w^2}, \quad Nu_x = \frac{\beta q_w}{\kappa(T_w - T_\infty)} \tag{9}$$

where $\tau_w = \mu(\partial u/\partial y)_{y=0}$ is the skin friction or the shear stresses and $q_w = -k(\partial T/\partial y)_{y=0}$ is the heat flux from the surface of the sheet. The dimensionless skin friction coefficient and Nusselt number are given as,

$$\mathrm{Re}_x^{1/2} c_f = f''(0), \quad \mathrm{Re}_x^{-1/2} Nu_x = (1+\psi)(-h'(0)) \tag{10}$$

where $\mathrm{Re}_x = U_w(x)x/a$ is the local Reynolds number.

TABLE 1. The features of thermo-physical hybrid nanofluids. (Source: Devi and Devi [32])

Features	Hybrid nanofluid
Density (ρ) unit	$\rho_{hnf} = (1-\phi_2)[(1-\phi_1)\rho_f + \phi_1\rho_{s1}] + \phi_2\rho_{s2}$
Viscosity (μ) unit	$\mu_{hnf} = \mu_f/(1-\phi_1)^{2.5}(1-\phi_2)^{2.5}$

Heat capacity (ρC_p) unit	$(\rho C_p)_{hnf} = (1-\phi_2)\left[(1-\phi_1)(\rho C_p)_f + \phi_1(\rho C_p)_{s1}\right] + \phi_2(\rho C_p)_{s2}$
Thermal conductivity (k) unit	$k_{hnf} = \frac{k_{s2} + 2k_{nf} - 2\phi_2(k_{nf} - k_{s2})}{k_{s2} + 2k_{nf} + \phi_2(k_{nf} - k_{s2})} \times k_{nf}$ With $k_{nf} = \frac{k_{s1}+2k_f-2\phi_1(k_f-k_{s1})}{k_{s1}+2k_f+\phi_1(k_f-k_{s1})} \times k_f$

TABLE 2. The values of nanoparticles and base fluid thermo-physical properties

Thermophysical properties	GO (Aminuddin et al. [33])	Fe_3O_4 (Lee et al. [34])	H_2O (Waini et al. [35])
$k\ (Wm^{-1}K^{-1})$ Thermal conductivity	5000	80	0.613
$\rho\ (kgm^{-2})$ Density	1800	4950	997.1
$C_p(Jkg^{-1}K^{-1})$ Specific heat	717	670	4179

RESULTS AND DISCUSSIONS

This part intends to shed light on the relationships between the local Nusselt number, the skin friction coefficient, velocity profiles, and temperature profiles. Nonlinear ordinary differential equations (Eqs. (6) and (7)) with boundary conditions (Eq. (8)) were numerically resolved using the bvp4c boundary value problem solver in the MATLAB software. The infinite value for $\eta \to \infty$ is set to $\eta = 25$, and the relative tolerance is set to 10^{-10} to regulate the precision of the numerical computation. Table 3 compares the numerical results to those found in previous publications by Nasir et al. [31], Rosca et al. [36], and El-Aziz [37] for the purpose of validating the results. All mathematical models will be reduced to hydrodynamic where $\varphi_a = \varphi_b = \varphi_c = \varphi_d = Q = 0$, the stagnation point flow over elonging and shrunk surface with the absence of all effects. Nasir et al. [31] and Rosca et al. [36] computed the solution by implementing bvp4c, while El-Aziz [37] solved using fifth-order Runge-Kutta-Fehlberg. The consistency of the outcomes demonstrates the validity of the current numerical findings. The validation process is essential to ensuring the numerical simulations' accuracy and reliability. The comparison with previous publications provides a benchmark for future studies and contributes to the advancement of the field. The computed solution for current results is comparable with Nasir et al. [31], Rosca et al. [36] and El-Aziz [37]. Hence, the present numerical findings are validated.

TABLE 3. Comparison of $f''(0)$ for $\varphi_a = \varphi_b = \varphi_c = \varphi_d = Q = S = 0$.

α	Current results		Nasir et al. [31]		Rosca et al. [36]		El-Aziz [37]	
	1st Solution	2nd Solution	1st Solution	2nd Solution	1st Solution	2nd Solution	1st Solution	2nd Solution
8.0	-21.68479964	-	-21.6847996	-	-	-	-	-
2.0	-1.88730664	-	−1.88730700	-	−1.887306	-	-	-
0.5	0.71329492	-	0.71329500		0.713294	-	-	-
0.0	1.23258760	-	1.23258800	-	1.232587	-	-	-
-0.25	1.40224066	-	1.4022408	-	1.402240	-	1.4022408	-
-1.0	1.32881680	0.0	1.3288168	0.0	1.328816	0.0	1.3288169	0.0
-1.20	0.93247312	0.23364968	0.9324733	0.233650	0.932473	0.233649	0.9324740	0.2336497
-1.2465	0.58427981	0.55429612	0.5842816	0.554296	0.584281	0.554292	0.5842915	0.5542856

It is essential to justify that Fe_3O_4 is the first nanoparticle and GO is the second nanoparticle. The Prandtl number is chosen to be 7.2, which means water. Nusselt number and skin friction values for various values of vital parameters are listed in Table 4. These values are essential for predicting the system's heat transfer and fluid flow characteristics. Researchers can use this information to optimise designs and improve performance. It is evident from Table 4 that the EMHD parameter significantly impacts the skin friction under the stimulus of the heat absorption effect. The drag

forces amplified as the magnetic field increased. This phenomenon happened because the EMHD helped to fasten the movement of the hybrid nanofluids' molecules while the fluid flow's inertia energy was imposed to maintain the activity. However, the second solution showed different behaviour from the first solution. These results indicated that, at some point, the drag forces would be diminished as the EMHD parameter was enlarged. The Nusselt number is also affected by the influence of the EMHD parameter. It is widely known that heat transfer will escalate when the molecules move faster; hence, the Nusselt number will also be aggravated. The hybrid nanofluids' molecules can quickly transport the heat from the surface and transmit it to far-field flow. Similar behaviour for the second solution of the Nusselt number was found. The trend cuts back as the EMHD parameter strengthens. It can also be observed that the radiation parameter has the most significant impact on the Nusselt number (for both solutions). The physical reason for this phenomenon is that the radiation will enhance the kinetic energy of the hybrid nanofluid's molecules, which allows for greater heat exchange in the far-field flow. Furthermore, the study suggests that the impact of radiation on the Nusselt number is more pronounced at higher temperatures due to the increased thermal energy available for radiation absorption. This finding highlights the importance of considering radiation effects in the heat transfer analysis of hybrid nanofluids at elevated temperatures. Observing how the system reacts to incoming and outgoing heat (fluid flow) is instructive. The Nusselt number increases for the first and second solutions as the heat absorption parameter increases, causing the molecules to transfer heat to the far-field flow more than usual. Further, the heat transfer rate will be elucidated. The impact of heat absorption and generation on the system (fluid flow) is worth seeing. The heat absorption parameter heightens the Nusselt number for the first and second solutions. It is due to the fact that heat absorption increased the ability of the hybrid nanofluid molecules to transmit the heat from the Riga plate surface towards the far-field flow. Meanwhile, the heat generation parameter at its value $\psi < 3.0$, the Nusselt number, is abatement. Still, as soon as the movement of the hybrid nanofluid's molecules stabilised, the heat transmittance rate increased significantly.

It is availed to disclose the performance between hybrid nanofluid GO-Fe_3O_4/H_2O with nanofluid Fe_3O_4/H_2O. Table 5 contains information about the effectiveness of GO-Fe_3O_4/H_2O and Fe_3O_4/H_2O of skin friction and Nusselt number with the essence of radiation and heat absorption/generation parameters. The first solution is without a bracket, while the second solution is in the bracket. The efficacy of GO-Fe_3O_4/H_2O for skin friction (heat absorption and generation) is intensified as the concentration of GO molecules is augmented in the fluid. The annexes are about 3.2% from the classical nanofluid Fe_3O_4/H_2O, and the percentage calculation is using

$$\left|\frac{\left(\mathrm{Re}_x^{1/2} c_f\right)_{\phi_2=0.01} - \left(\mathrm{Re}_x^{1/2} c_f\right)_{\phi_2=0.0}}{\left(\mathrm{Re}_x^{1/2} c_f\right)_{\phi_2=0.0}}\right| \times 100\% . \tag{11}$$

The influence of heat absorption and heat generation parameters produced similar behaviour towards the Nusselt number. Both parameters reduced the Nusselt number slightly. The improvement is about 1.6% from the nanofluid performance, and the percentage calculation is similar to equation (11).

TABLE 4. Values of skin friction $\mathrm{Re}_x^{1/2} c_f$ and Nusselt number $\mathrm{Re}_x^{-1/2} Nu_x$ for $\phi_1 = 0.01, \phi_2 = 0.001, \alpha = -2.5, S = 2.0, \mathrm{Pr} = 7.2, \omega = 1.0$.

Q	χ	ψ	$\mathrm{Re}_x^{1/2} c_f$		$\mathrm{Re}_x^{-1/2} Nu_x$	
			1st solution	2nd solution	1st solution	2nd solution
0.1	5.0	-2.0	5.795921982	0.733693220	1.493683324	1.374126013
0.5			6.241349243	0.630627216	1.500591164	1.365959839
2.0			7.681313006	0.555046090	1.521796815	1.337883636
0.5	5.0	-2.0	6.241349243	0.630627216	1.500591164	1.365959839
	10.0		6.241349243	0.630627215	2.025791403	1.876479028
	15.0		6.241349243	0.630627215	2.464345087	2.308180190
0.5	5.0	-1.0	6.241349243	0.630627215	1.189042712	1.033695143
		-2.0	6.241349243	0.630627216	1.500591164	1.365959839
		-3.0	6.241349243	0.630627215	1.760782749	1.639716773
		1.0	6.241349243	0.630627215	0.161017563	-0.136369409
		2.0	6.241349243	0.630627215	-1.423163600	-2.522492011
		3.0	6.241349243	0.630627215	8.757463183	4.351266948

TABLE 5. Values of skin friction $\mathrm{Re}_x^{1/2} c_f$ and Nusselt number $\mathrm{Re}_x^{-1/2} Nu_x$ for $\phi_1 = 0.01, \alpha = -3.0, S = 2.0, \mathrm{Pr} = 7.2, \omega = 1.0, Q = 1.0, \omega = 1.0$ with varies of the value of radiation.

χ	$\mathrm{Re}_x^{1/2} c_f \quad (\psi = -0.2, 0.2)$			$\mathrm{Re}_x^{-1/2} Nu_x \quad (\psi = -0.2)$			$\mathrm{Re}_x^{-1/2} Nu_x \quad (\psi = 0.2)$		
	$\phi_2 = 0.0$	$\phi_2 = 0.001$	$\phi_2 = 0.01$	$\phi_2 = 0.0$	$\phi_2 = 0.001$	$\phi_2 = 0.01$	$\phi_2 = 0.0$	$\phi_2 = 0.001$	$\phi_2 = 0.01$
5.0	6.080062533 [2.17247264]	6.060585751 [2.17888559]	5.883133885 [2.23863793]	0.832563249 [0.71614482]	0.831662003 [0.71594064]	0.823463241 [0.71417675]	0.626093922 [0.49167208]	0.625108549 [0.49147463]	0.616136432 [0.48978828]
10.0	6.080062533 [2.17247264]	6.060585751 [2.17888559]	5.883133885 [2.23863793]	1.123845880 [1.00163775]	1.122914333 [1.00141245]	1.114430400 [0.99946696]	0.850185847 [0.71307970]	0.849152247 [0.71282910]	0.839738052 [0.71067126]
15.0	6.080062533 [2.17247264]	6.060585751 [2.17888559]	5.883133885 [2.23863793]	1.366094417 [1.24248650]	1.365149364 [1.24224721]	1.356542277 [1.24018010]	1.048936557 [0.91361049]	1.047900283 [0.91334247]	1.038465130 [0.91103000]

Fig. 2(a) shows the consequence of the EMHD parameter on the GO-Fe_3O_4/H_2O flow velocity for the shrunk Riga plate surface. For the dual solutions, EMHD parameter rise causes a decline in the momentum boundary layer width. Because of the suction action on the system and the magnetic field of the Riga plate, the hybrid nanofluid molecules are forced to travel more quickly, snowballing the GO-Fe_3O_4/H_2O flow's velocity even while the surface is contracting. As a result of the system suction parameter's implementation, it indicates that the drag force does not impact the fluid flows. The temperature curve is shown in Fig. 2(b) for various values of the EMHD parameter. As the EMHD parameter rises, the temperature and the thermal boundary layer thickness typically drop. This phenomenon is due to the fluid molecules flowing more quickly, effectively carrying heat away from the surface more rapidly than when they were stationary, and vice versa. As a result, the temperature will drop while the heat transfer rate will upsurge. The red line in Fig. 2(b) reflects the results with the heat generation, which contributes heat to the system, whereas the blue line represents the findings with heat absorption, which absorbs heat from the system.

It is eye-catching that the thickness of the Riga plate played an essential part in the flow and heat transmission in the system. Fig. 3(a) illustrates the magnifying of Riga plate thickness which affected the velocity of the GO-Fe_3O_4/H_2O to lose speed. It is due to the fact that the size of the Riga plate influences the forte of the magnetic field produced. The strength diminishes as the thickness is augmented. Hence the velocity of the GO-Fe_3O_4/H_2O flow is declining. This occurrence also affected the temperature profile, as depicted in Fig. 3(b). Remarkably, heat generation and absorption parameters proliferated the temperature profile for GO-Fe_3O_4/H_2O. Since the movement of the hybrid nanofluid molecules slows down, the heat accumulates in the system, cumulative the temperature profile.

The discovery of the influence of radiation towards temperature profile is adorned in Fig. 4. It is evident that when radiation's value rises, the temperature distribution widens. The thermal boundary layer's width is also augmented for higher radiation values. This phenomenon is because interatomic collisions can affect the kinetic energy of a fluid molecule, which in turn improves the fluid's temperature distribution. This behaviour is displayed by both heat generation and heat absorption.

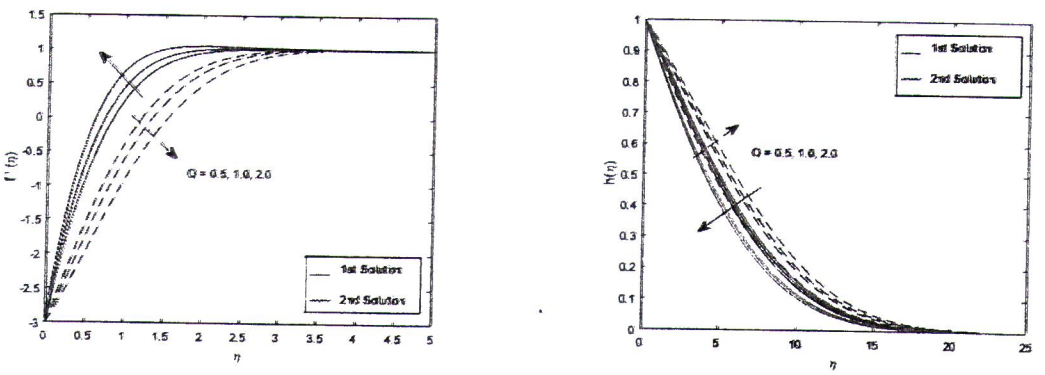

(a) (b)

FIGURE 2. Variation of (a) velocity profile $(\psi = -0.2, 0.2)$ and (b) temperature profile $(\psi = -0.2[\text{red}], 0.2[\text{blue}])$ for $\text{Pr} = 7.2, \chi = 5.0, \omega = 1.0, S = 2.0, \alpha = -3.0$.

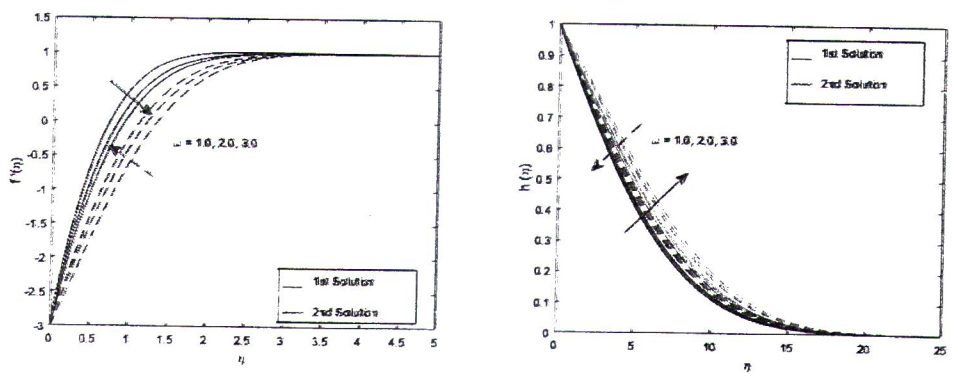

(a) (b)

FIGURE 3. Variation of (a) velocity profile $(\psi = -0.2, 0.2)$ and (b) temperature profile $(\psi = -0.2[\text{red}], 0.2[\text{blue}])$ for $\text{Pr} = 7.2, \chi = 5.0, Q = 1.0, S = 2.0, \alpha = -3.0$.

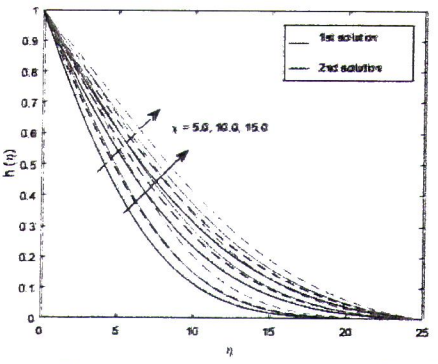

FIGURE 4. Variation of temperature profile $(\psi = -0.2[\text{red}], 0.2[\text{blue}])$ for $\text{Pr} = 7.2, \omega = 1.0, Q = 1.0, S = 2.0, \alpha = -3.0$.

CONCLUSION

The EMHD stagnation points GO-Fe_3O_4/H_2O hybrid nanofluid flow and heat transfer over porous moving Riga plate are investigated. The effect of radiation, EMHD, the thickness of the Riga plate, and heat absorption/generation are also being considered. Implementing an appropriate similarity variable transforms mathematical modelling into an ordinary differential equation. The bvp4c solver is implemented to solve the mathematical model. The thorough analysis of the computed results provides insights into the behaviour of the model and its suitability for real-world applications. The crucial findings are listed as follows:

- The skin friction and Nusselt number can be controlled to augment with EMHD, radiation, heat generation and thickness of the Riga plate parameters.
- The velocity profiles are found to be amplified together with EMHD while depreciated with the thickness of the Riga plate parameter.
- Temperature profiles will be increasing by intensifying the values of radiation, heat generation/absorption and thickness of the Riga plate. However, EMHD parameters can reduce the temperature profile.
- The performance of GO-Fe_3O_4/H_2O hybrid nanofluid for skin friction is found to be about 3.2%, while the Nusselt number performance is about 1.6% from Fe_3O_4/H_2O classical nanofluid.

This study exhibits considerable potential for advancing the current findings by exploring the impacts of various nanoparticles, their concentrations, and sizes within the nanofluid. Additionally, it is recommended to conduct optimisation analyses in order to determine the optimal parameters that can enhance heat transfer and fluid flow within the system. Furthermore, it is prudent to investigate the influence of uncertainties in input parameters and boundary conditions on the outcomes of the simulation. Incorporate uncertainty quantification methodologies to evaluate the robustness of your results and enhance the comprehensiveness of your understanding regarding the behaviour of the system.

ACKNOWLEDGEMENTS

The authors would like to thank the Ministry of Higher Education Malaysia and the National Defence University of Malaysia for supporting this research. This research was funded by the Ministry of Higher Education Malaysia, Fundamental Research Grant Scheme, grant number FRGS/1/2021/STG06/UPNM/02/1.

REFERENCES

1. M. Hemmat Esfe, M. Bahiraei, H. Hajbarati and M. Valadkhani, Appl. Therm. Eng., **178**, 115487 (2020).
2. Z. Narankhishig, J. Ham, H. Lee and H. Cho, Appl. Therm. Eng., **193**, 116987 (2021).
3. A. Olabi, K. Elsaid, E.T. Sayed, M.S. Mahmoud, T. Wilberforce, R.J. Hassiba and M.A. Abdelkareem, Nano Energy, **84**, 105871 (2021).
4. M. Modak, S. Srinivasan, K. Garg, S.S. Chougule, M.K. Agarwal and S.K. Sahu, Chem. Eng. Process., **91**, 104-113 (2015).
5. M. Shanmugam, S. Sathiyamurthy, G. Rajkumar, S. Saravanakumar, S. Tamil Prabakaran and V.S. Shaisundaram, Mater. Today-Proc., **37**, 1943-1956 (2021).
6. M.A. Nazari, R. Ghasempour, M.H. Ahmadi, G. Heydarian and M.B. Shafii, Int. Commun. Heat Mass, **91**, 90 – 94 (2018).
7. B. Sun, Y. Zhang, D. Yang and H. Li, Appl. Therm. Eng., **151**, 556–566 (2019).
8. R.R. Sahoo, Heat Mass Transfer, **56**, 3023–3033 (2020).
9. M. Gupta, V. Singh and Z. Said, Sustain. Energy Technol. Assess., **39**, 100720 (2020).
10. B.R. Ponangi, V. Krishna and K.N. Seetharamu, Int. J. Therm. Sci., **165**, 106925 (2021).
11. S.M. Hussain, R. Sharma and A.J. Chamkha, Chinese, J. Phys. **75**, 120–138 (2022).
12. U.K. Sur, Int J Electrochem, **2012**, 237689 (2012).
13. A.A. Balandin, S. Ghosh, W. Bao, I. Calizo, D. Teweldebrhan, F. Miao and C.N. Lau, Nano Lett., **8**, 902-907 (2008).
14. M.L. Yola, N. Atar, T. Eren, H. Karimi-Maleh and S. Wang, RSC Adv., **5**, 65953-65962 (2015).
15. R. Tarcan, O. Todor-Boer, I. Petrovai, C. Leordean, S. Astilean and I. Botiz, J. Mater. Chem. C, **8**, 1198-1224 (2020).
16. N.K. Mahanta and A.R. Abramson, 13th InterSociety Conference on Thermal and Thermomechanical Phenomena in Electronic Systems, IEEE, 1-6 (2012).
17. J. Liu, Z. Ye, L. Zhang, X. Fang and Z. Zhang, Sol. Energ. Mat. Sol. C., **136**, 177-186 (2015).
18. S. Torii, Mater. Today-Proc., **35**(3), 506-511 (2021).
19. S. Nasir, A.S. Berrouk, A. Aamir, T. Gul and I. Ali, Heliyon, **9**(4), e15089 (2023).
20. H. Masuda, A. Ebata, K. Teramae and N. Hishinuma, Netsu Bussei, **7**, 227-233 (1993).
21. B. Sun, W. Lei and D. Yang, Int. Commun. Heat Mass, **64**, 21-28 (2015).
22. R. Walvekar, M.K. Siddiqui, S. Ong and A.F. Ismail, J. Exp. Nanosci., **11**(1), 1-17 (2016).
23. P.S. Reddy and A.J. Chamkha, Adv. Powder Technol. **27**, 1207–1218 (2016).
24. M. Khan, M. Azam and A.S. Alshomrani, Int. J. Heat Mass Tran., **110**, 437-446 (2017).
25. M. Ishaq, G. Ali, Z. Shah, S. Islam, and S. Muhammad, Entropy, **20**, 412 (2018).
26. M. VeeraKrishna and A.J. Chamkha, Phys. Fluids **30**, 053101 (2018).
27. F. Mebarek-Oudina, Heat Tran-Asian Res., **48**, 135-147 (2019).
28. H. Waqas, U. Farooq, D. Liu, M. Abid, M. Imran and T. Muhammad, Int. Commun. Heat Mass, **138**, 106303 (2022).
29. A.M. Rashad, M.A. Nafe and D.A. Eisa, Arab J Sci Eng., **48**, 939-952 (2023).
30. M.Z.H. Supian, N.A.A.M. Nasir and A. Ishak, Magnetohydrodynamics **57**, 405-416 (2021).
31. N.A.A.M. Nasir, A. Ishak and I. Pop, J. Zhejiang Univ-Sc. A **20**, 290–299 (2019).
32. S.P.A. Devi and S.S.U. Devi, Int. J. Nonlin. Sci. Num., **17**(5), 249-257 (2016).
33. N.A. Aminuddin, N.A.A.M. Nasir, W. Jamshed, A. Ishak, I. Pop and M.R. Eid, Symmetry **15**, 584 (2023).
34. A. Lee, C. Veerakumar, H. Cho, Appl. Sci.-Basel, **11**, 4683 (2021).
35. I. Waini, A. Ishak and I. Pop, Int. J. Numer. Method H. **29**(9), 3110-3127 (2019).
36. A.V. Rosca, N.C. Rosca and I. Pop, Int. J. Numer. Method H., **26**(1), 348-364 (2016).
37. M.A. El-Aziz, J. Egypt. Math. Soc., **24**(3), 479-486 (2016).